# Insights into $CO_2$ and $CH_4$ Adsorption by Pristine and Aromatic Amine-Modified Periodic Mesoporous Phenylene-Silicas

*Mirtha A. O. Lourenço,[a] Christophe Siquet,[b,*] João Santos,[b] Miguel Jorge,[c] José R. B. Gomes,[d] Paula Ferreira[a,*]*

[a]CICECO, Departament of Materials and Ceramic Engineering, University of Aveiro, Campus Universitário de Santiago, 3810-193 Aveiro, Portugal.

[b]LSRE, Faculty of Engineering, University of Porto, Rua Dr. Roberto Frias, s/n, Porto, Portugal.

[c]Department of Chemical and Process Engineering, University of Strathclyde, 75 Montrose Street, Glasgow G1 1XJ, United Kingdom.

[d]CICECO, Department of Chemistry, University of Aveiro, Campus Universitário de Santiago, 3810-193 Aveiro, Portugal.

Corresponding Authors*

Phone: +351 234 401419; fax: +351 234 401470;

*E-mail addresses: csiquet@fe.up.pt (C. Siquet); pcferreira@ua.pt (P. Ferreira)*

**Abstract**

The synthesis and characterization of pristine and amine-functionalized periodic mesoporous phenylene-silicas having different pore sizes are reported. We explore the potential of these materials for $CO_2/CH_4$ separation, by studying the adsorption of pure $CO_2$ and pure $CH_4$ gases. The aminated periodic mesoporous phenylene-silica with the smallest pore size is the best adsorbent to $CO_2$, presenting a Henry's constant of 0.56 $mol \cdot kg^{-1} \cdot bar^{-1}$ at 35 ºC. However, the corresponding Henry's constant for $CH_4$ is extremely low (0.06 $mol \cdot kg^{-1} \cdot bar^{-1}$ at 35 ºC). It is observed a direct correlation between the % of $T^2_{SMP}$ silanols species and the values of the Henry's constants, which may be used to theoretically predict experimental $CO_2$ Henry's constants of potential adsorbents.

## 1. Introduction

The world energy demands have been increasing in the last decades, driven by strong economic growth and expanding populations. Alternative energy resources have been proposed to satisfy part of the energy supplies. Biogas is an alternative energy source, produced through the anaerobic digestion process of organic matter, such as sewage, animal byproducts, and agricultural, industrial, and municipal solid waste.[1–7] Biogas is composed mainly by methane (60 - 70 %) and carbon dioxide (30 - 40 %) and presents traces of $H_2S$, CO, $H_2$ and $N_2$. Thus, $CO_2$ is the major contaminant and its separation from methane is the most critical step in biogas upgrading.[1–4,8,9] The purified biogas (enriched in methane) has high interest once it can be used for household applications, fuel vehicles or electricity generation.[1] The commercial solutions available for $CO_2$ uptake from biogas use absorption process through the use of amine solvents such as monoethanol amine (MEA), diethanolamine (DEA) or methyl diethanolamine (MDEA), which are able to interact chemically with $CO_2$. The available commercial technologies to $CO_2/CH_4$ separation present several drawbacks associated with: i) the low $CO_2$ loading capacity of the solvent; ii) the degradation of the amine solvent in contact with gases as for example $NO_x$, $SO_x$, $O_2$ gases; iii) the high cost of solution regeneration; iv) the corrosion of the equipment by the amine solution and v) the scale up of the equipment used.[10] Therefore, an energy efficient process to uptake the $CO_2$ contaminant from $CH_4$ is required for the wide application of biogas with the purpose of increasing the purity and also to avoid the corrosion of equipment and pipelines promoted by the acid $CO_2$ gas.[11,12] Moreover, up-taken $CO_2$ can be then used as an effective refrigerant.[1,13] Current methodologies to purify off-gas (the effluent gas produced from the anaerobic digestion process of organic matter) and to increase its caloric value[1] are absorption, cryogenic distillation, membrane separation, and

adsorption.[13] The latter is a very attractive technique from small to medium-scale operations, but relies on the availability of highly effective adsorbent materials.

The development of adsorbents to uptake the $CO_2$ gas from biogas *via* adsorptive separation involves the preparation of materials with different nature and structure.[14] Various mesoporous and microporous adsorbents (carbons[15–19], MOFs[15,20,21], zeolites[11,15,22–25], clays[26,27], and silica-based mesoporous materials[28,29]) have been proposed for $CO_2$ adsorption/separation from biogas. Although, these adsorbents are still not ideal for $CO_2$ uptake from biogas mainly due to their unsatisfactory performances. Thus, the ideal adsorbent is still undiscovered and needs to present all optimal features as, for instance, high capacity, perfect selectivity, long-term durability, stability, fast uptake processes and easy regeneration consistent with negligible capacity loss on multiple adsorption/desorption cycles.[30] In an attempt to achieve this, we are exploring the possibility of applying periodic mesoporous phenylene-silicas (PMOs)[31–33] as adsorbents for $CO_2/CH_4$ gas separation. The interest to use PMOs as adsorbents in this field relies in the assumption that these materials possess high specific surface areas, high pore volumes and are easy to be modified.[31–37] Additionally, PMOs also have the advantages of exhibiting meso- and molecular-scale periodicities that can promote a good diffusion of the molecules (the adsorbates but also the reagents required to modify the PMOs) within the channels. PMOs possess both the increased organization of the pores and the presence of the organic functions (such as ethylene, phenylene, biphenylene, etc.) that are well integrated in the walls. Moreover, PMOs are characterized by alternating organic-inorganic groups along the pore wall, which assign alternating hydrophobic-hydrophilic character. Furthermore, it is possible to control the porosity of the PMOs using the template-assisted self-assembly method.[31–37] All of the features above increase the attractiveness of PMOs as potential adsorbents for $CO_2/CH_4$

adsorption/separation. Recently, alkyl amine functionalities (more specifically the *N*-[3-(trimethoxysilyl)propyl]-ethylenediamine) grafted on the silanols of phenylene-bridged PMO and of SBA-15 were tested in the adsorption of pure $CO_2$ at 25 °C in a pressure range up to 1.2 atm.[38] It was observed that the alkyl amine-PMO adsorbs a larger amount of $CO_2$ at a faster adsorption rate when compared with SBA-15, which demonstrates that the functionalization of PMOs with amines is more relevant than a similar degree and nature of functionalization in silica for the adsorption of $CO_2$. Interestingly, the unmodified SBA-15 silica also adsorbs a smaller amount of $CO_2$ when compared with the unmodified PMO. This behavior was explained by the higher hydrophobicity of the PMO pore wall when compared with that of SBA-15. Hence, water adsorption is expected to be more acute in SBA-15 than in PMO materials, competing more with $CO_2$ for available adsorption sites on the former class of materials, so, organosilica instead of pure silica supports were proposed for immobilization of amines groups aiming materials for $CO_2$ adsorption/separation.[38] Despite the fact that PMOs are more expensive than silica, the superior ability of amine modified PMOs to adsorb $CO_2$ can be transferred and should be explored for these application.

Here, we considered the phenylene-bridged PMOs as potential candidates for the $CO_2/CH_4$ separation. In this way, phenylene-bridged PMO with different pore sizes were prepared by changing the alkyl chain length of the cationic surfactant[39] since the pore size and pore curvature may play an important role on the diffusion of the reagents or gas molecules inside the pores. Additionally, the amount of amine functionalities into the materials, their locations and the type of silanols are certainly important variables on the adsorptive properties of these materials. So, after the synthesis of the PMOs, the mono-nitration of the benzyl bridges was performed with nitric acid in the presence of sulfuric

acid. Then, the nitro group was reduced to the amine in the presence of tin chloride and hydrochloric acid.[40] To the best of our knowledge, the amination of the phenylene bridge in the $C_n$-PMOs with $n < 18$, was not attempted before. Hence we describe for the first time the synthesis and characterization of aromatic amine-funtionalized PMOs with pore sizes ranging from 2.4 and 3.7 nm. All materials are tested on the $CO_2$ and $CH_4$ adsorption. The physicochemical characterization is performed to fully understand the potential of these materials for $CO_2/CH_4$ separation.

## 2. Experimental section

### 2.1. Chemicals and Reagents

Dodecyltrimethylamonium bromide ($C_{12}$-TMA, 99%, Aldrich), tetradecyltrimethylammonium bromide ($C_{14}$-TMA, 99%, Aldrich), hexadecyltrimethylammonium bromide ($C_{16}$-TMA, 95%, Aldrich), octadecyltrimethylammonium bromide ($C_{18}$-TMA, 98%, Aldrich), ethanol (PA, Panreac), hydrochloric acid (HCl, 37% v/v, Carlo Erba), nitric acid ($HNO_3$, 65% v/v, Panreac), sulfuric acid ($H_2SO_4$, 95-97% v/v, Panreac), tin chloride ($SnCl_2$, 98%, Aldrich) and isopropylamine (>99.5%, Aldrich) were purchased from commercial sources. All chemicals were used as received.

### 2.2. Materials synthesis

#### 2.2.1. $C_n$-PMO adsorbents preparation

Phenylene-bridged PMOs with different pore sizes (hereafter denoted $C_n$-PMOs, $n$ = 12, 14, 16 or 18) were prepared following procedures previously described in literature.[39,41] The 1,4-bis(triethoxysilyl)benzene (BTEB) precursor[42] is hydrolyzed and condensed

around a surfactant, the $C_n$-trimethylammonium bromide template ($C_n$-TMA, $n$ =12, 14, 16 or 18), Scheme 1.

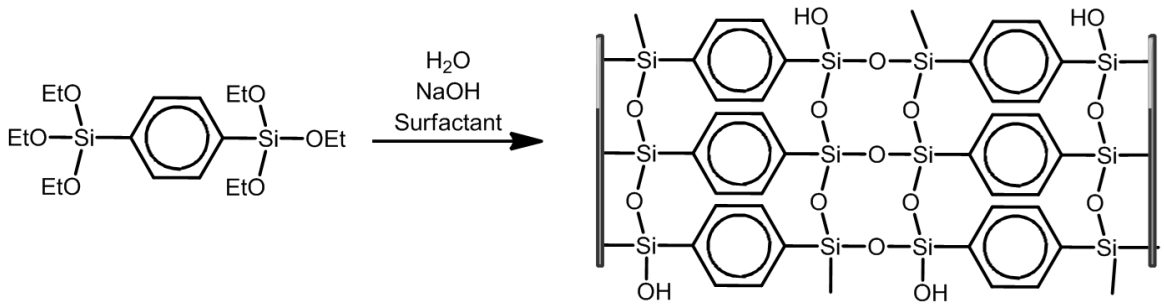


**Scheme 1.** Synthesis route for $C_n$-PMOs, $n$ = 12, 14, 16 and 18, prepared with $C_{12}$-TMA, $C_{14}$-TMA, $C_{16}$-TMA and $C_{18}$-TMA surfactants, respectively.

In a typical synthesis of the $C_n$-PMO materials, the surfactant is dissolved in a mixture of distilled water and 6 M aqueous sodium hydroxide at 20 – 60 °C. BTEB was subsequently added dropwise under vigorous stirring, at room temperature. The molar ratio BTEB : water is always constant and equal to 1 : 531 (molar ratio corresponding only to the distilled water), with the quantities of surfactant and NaOH adjusted according to the surfactant used (c.f. Table 1). The mixture was kept for 20 minutes in an ultrasonic bath (Bransonic ultrasonic cleaner 1510E-DTH). The reaction mixture was stirred for 24 hours at room temperature, and was then transferred into a Teflon lined autoclave for additional 24 hours at 100 °C. The final precipitate was recovered by filtration, washed with warm distilled water and dried at 60 °C.

To obtain porous PMO materials, the surfactants were removed through solvent extraction.[31–33,39,41] An aliquot of 0.5 g of the as-synthesized powder was stirred in a solution of 4.5 g of 37% HCl and 125 mL ethanol, for 8 hours at 80 °C. The powder was

filtered off, washed with ethanol and water and dried overnight at 60 °C. The confirmation of the template removal was made through $^{13}C$ NMR spectroscopy and TGA analysis.

**Table 1.** Molar ratio of the surfactant and NaOH for each $C_n$-PMO in relation to the BTEB precursor.

| | **$C_{18}$-PMO** | **$C_{16}$-PMO** | **$C_{14}$-PMO** | **$C_{12}$-PMO** |
|---|---|---|---|---|
| **Surfactant** | 0.96 | 1 | 1.05 | 1.4 |
| **NaOH** | 4.05 | 3.85 | 3.65 | 3.04 |

### 2.2.2. $NH_2$-$C_n$-PMO adsorbents preparation

The amine phenylene-modifications (to prepare $NH_2$-$C_n$-PMO, $n$ =12, 14, 16 or 18) were made using the same two-step procedure reported by Inagaki *et al*.[40] First a strong acid treatment with $HNO_3/H_2SO_4$ was used to incorporate the nitro groups into the phenylene moieties of PMO followed by treatment with $SnCl_2$/HCl to reduce the nitro groups to the desired amine functionalities (Scheme 2).

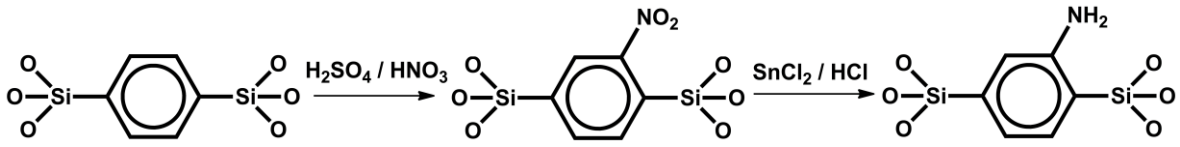


**Scheme 2.** Synthesis route for the amine functionalization of the $C_n$-PMOs, $n$=12, 14, 16 and 18.

### 2.3. Materials characterization

All PMO materials were evaluated by powder X-ray diffraction (PXRD), $N_2$-sorption and transmission electron microscopy (TEM). The chemical properties of the materials were evaluated by elemental analysis (EA), $^{13}C$, $^{15}N$ and $^{29}Si$ solid-state nuclear

magnetic resonance (NMR) and Fourier transformed infrared (FTIR) spectroscopies. The thermal stability was evaluated by thermogravimetric analyses (TGA). More information concerning the measurements (specific methods, equipment models and conditions used) is available in the supporting information (SI).

### 2.4. Adsorption measurement procedure

Adsorption isotherms of carbon dioxide and methane were measured on as-synthesized and amine-modified PMO materials, at 308 K and pressures up to 2 bar, using an in-house built manometric apparatus, Figure S1. The samples were activated, according to the heating program shown in Figure S2 (first at 80 °C during 5 hours and then at 160 °C during 10 hours), under vacuum of ca. 14 mbar. The $CO_2$ and $CH_4$ gases were used as provided by Air Liquide (France), with a purity of 99.998 % and 99.95 % respectively.

The experimental adsorption measurement technique adopted was previously described[43] and is shortly summarized here. Before performing each adsorption measurement, the void volume was determined by Helium picnometry, as described in our previous publication (43). To perform an adsorption experiment, the gas to be adsorbed is fed into the gas tank until an initial pressure P is reached while the sample is kept isolated, in another tank, by a closed valve. After the gas feed, the pressure in the gas tank is allowed to stabilize over a given period of time. The adsorption process starts when the valve isolating the sample is opened, and a pressure decrease is observed until a plateau is reached. Pressure and temperature readings are constantly recorded over time, so that the adsorption uptake can be computed as a function of time. This procedure is repeated

sequentially for different values of pressure, starting from the previously equilibrated pressure point.

Each experimental pure component adsorption isotherm was fitted to a Langmuir model. The fitting parameters were then used to calculate the Henry's constant of adsorption ($K_H$, in mol·kg$^{-1}$·bar$^{-1}$) for each gas and each adsorbent by taking the slope of the isotherm in the limit of zero coverage. The Henry constant thus measures the affinity of each gas toward the solid surface. The Langmuir equation is expressed in Equation 1:

$$q = \frac{qs \times b \times P}{1 + b \times P} \qquad \text{(Equation 1)}$$

where $q$ is the amount adsorbed, $q_S$ is the Langmuir saturation capacity, $b$ is the Langmuir surface affinity parameter and $P$ is the pressure.

We then estimated the low-coverage $CO_2$ selectivity ($S$) of each material by taking the ratio of the Henry's constants for the two gases (Equation 2):

$$S^{CO2/CH4} = \frac{K_H^{CO2}}{K_H^{CH4}} = \frac{q_s^{CO2} \times b^{CO2}}{q_s^{CH4} \times b^{CH4}} \qquad \text{(Equation 2)}$$

## 3. Results and Discussion

### 3.1. Characterization of Materials

The structural order of the non-modified samples was studied by PXRD. Figure 1a (SI) shows the PXRD patterns of surfactant-free $C_{12}$-PMO, $C_{14}$-PMO, $C_{16}$-PMO and $C_{18}$-PMO samples. The patterns are in agreement with those reported in previous studies,[39,41] being compatible with a two-dimensional hexagonal symmetry (*p6mm*) lattice. The *d* spacing of the strong low-angle (100) reflection changes slightly from sample to sample. The lattice parameters, *a,* calculated from the $2\theta$ values of the (100) peaks for the

surfactant-free $C_{12}$-PMO, $C_{14}$-PMO, $C_{16}$-PMO and $C_{18}$-PMO materials are 4.14; 4.32; 4.76; and 5.36 nm, respectively (Table 2). The increase of the lattice parameters results in larger pore sizes (Figure 1d) as a function of the alkyl-tail lengths.

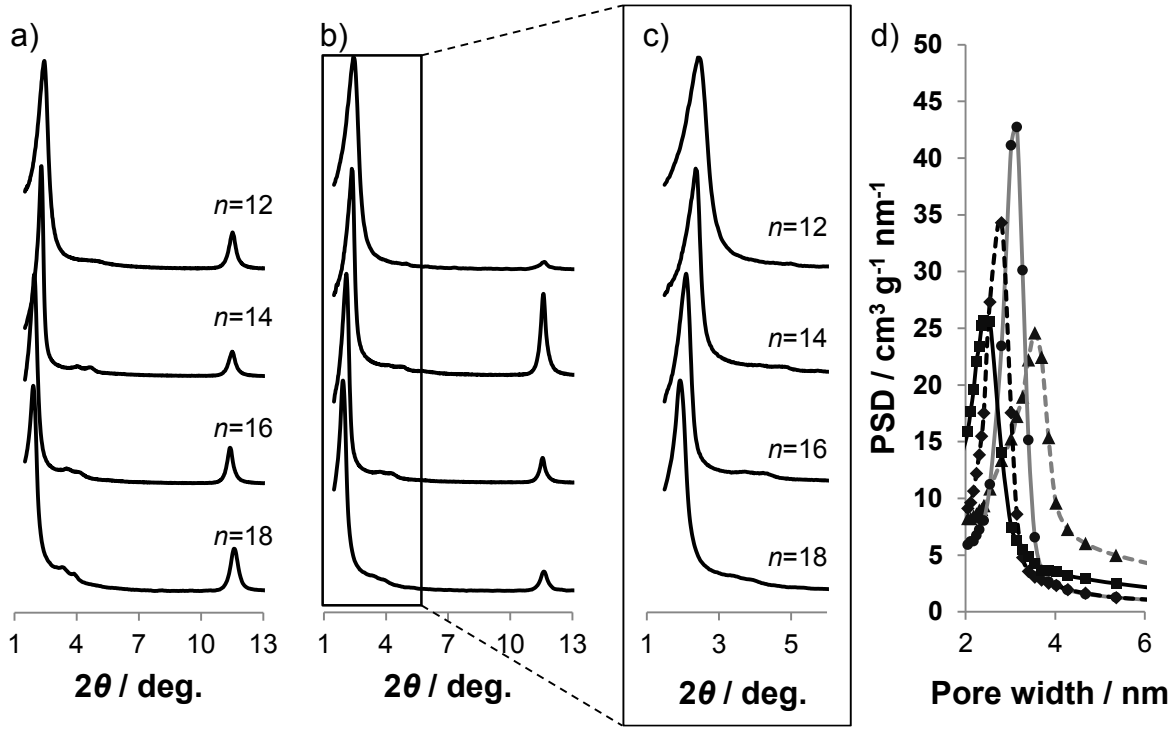


**Figure 1.** PXRD patterns of the: a) $C_n$-PMOs; b) and c) $NH_2$-$C_n$-PMOs. Pore size distribution profiles (d) calculated from the $N_2$ adsorption isotherm for $NH_2$-$C_{12}$-PMO (squares, black line); $NH_2$-$C_{14}$-PMO (rhombus, black dashed line); $NH_2$-$C_{16}$-PMO (circles, grey line); and $NH_2$-$C_{18}$-PMO (triangles, grey dashed line).

Table 2. Structural properties of $C_n$-PMOs and $NH_2$-$C_n$-PMOs materials. Pore parameters obtained from X-ray diffraction patterns and nitrogen sorption data.

| Sample | $d_{100}$ / nm | $a$ / nm[a] | $S_{BET}$ / $m^2$ $g^{-1}$ | $V_P$ / $cm^3$ $g^{-1}$ | $d_P$ / nm[b] | $b$ / nm[c] |
|---|---|---|---|---|---|---|
| $C_{12}$-PMO | 3.59 | 4.14 | 1004 | 0.14 | 2.54 | 1.60 |
| $NH_2$-$C_{12}$-PMO | 3.63 | 4.19 | 924 | 0.23 | 2.41 | 1.78 |
| $C_{14}$-PMO | 3.74 | 4.32 | 843 | 0.24 | 2.80 | 1.52 |
| $NH_2$-$C_{14}$-PMO | 3.79 | 4.37 | 778 | 0.16 | 2.80 | 1.57 |
| $C_{16}$-PMO | 4.12 | 4.76 | 832 | 0.45 | 3.14 | 1.62 |
| $NH_2$-$C_{16}$PMO | 4.22 | 4.88 | 623 | 0.33 | 3.14 | 1.74 |

| | | | | | | |
|---|---|---|---|---|---|---|
| $C_{18}$-PMO | 4.65 | 5.36 | 782 | 0.68 | 3.70 | 1.66 |
| $NH_2$-$C_{18}$-PMO | 4.62 | 5.34 | 719 | 0.55 | 3.54 | 1.80 |

[a]Unit cell parameter calculated as ($2d_{100}/\sqrt{3}$) . [b]Pore width obtained from the BJH method with the corrected Kelvin equation, i.e. KJS–BJH method at the maximum of pore size distribution calculated on the basis of adsorption data. [c]Pore wall thickness calculated as ($2d_{100}/\sqrt{3}$ - $d_P$), where the first term is the unit cell parameter.

The evidence for the hexagonal arrangement of the pores is obtained from the presence of the tiny (110) and (200) low-angle reflections observed in Figure 1a.[39,41] In addition to the low-angle peaks, the PXRD patterns display medium-range reflection at $d \sim 0.76$ nm, due to molecular-scale periodicity in the PMO pore walls along the channel direction.[41] The four different samples display these peaks at exactly the same *d* spacing, which is in agreement with Bion *et al.*[39] Thus the non-modified PMOs materials exhibit molecular-scale periodicity in the walls and, in addition, have different pore sizes. The structural order of the aminated samples was studied by PXRD and $N_2$ adsorption–desorption isotherms. Figure 1b and c shows the PXRD patterns of $NH_2$-$C_n$-PMO materials. As in the simple PMOs, the first strong low-angle (100) reflection peak associated to the (110) and (200) small reflections are characteristic of a two-dimensional hexagonal symmetry (*p6mm*) lattice, Figures 1b and c. Thus, the hexagonal arrangement is maintained upon amination.

The *d* spacings in the aminated samples are similar to the *d* spacings of the pristine PMOs. The lattice parameters, a, of the hexagonal array of mesopores obtained for the $NH_2$-$C_{12}$-PMO, $NH_2$-$C_{14}$-PMO, $NH_2$-$C_{16}$-PMO and $NH_2$-$C_{18}$-PMO materials are 4.19, 4.37, 4.88 and 5.34 nm, respectively, which means that the presence of the amino group does not significantly change those values relatively to the pristine materials (Table 2). In addition to the low-angle peaks, the PXRD patterns of all aminated samples display medium-range reflections at $d \sim 0.76 \pm 0.002$ nm, which are identical to that of the initial PMO materials,

implying that amination also did not significantly change the molecular-scale periodicity of the pore walls.

The presence of different mesopore sizes was confirmed by low temperature (-196 °C) $N_2$ adsorption–desorption experiments. In Figure S3 (SI), the samples display a type IV isotherm (IUPAC classification), usually observed for conventional mesoporous materials such as MCM-41, indicating mesopores of uniform size. The introduction of the amine into the mesochannels is confirmed by the reduction of the specific surface area ($A_{BET}$). The $NH_2$-$C_{12}$-PMO, $NH_2$-$C_{14}$-PMO, $NH_2$-$C_{16}$-PMO and $NH_2$-$C_{18}$-PMO materials present $A_{BET}$ of 924, 778, 623 and 719 $m^2 \cdot g^{-1}$, respectively (Table 2). A comparison of the pore size distribution (PSD) curves of $NH_2$-$C_{12}$-PMO, $NH_2$-$C_{14}$-PMO, $NH_2$-$C_{16}$-PMO and $NH_2$-$C_{18}$-PMO materials reveals a maximum shifting from 2.4 to 3.5 nm (Figure 1d and Table 2), respectively.

TEM images (Figure S4a, SI) reveal the high order along the channels for the $NH_2$-$C_{18}$-PMO, $NH_2$-$C_{16}$-PMO, $NH_2$-$C_{14}$-PMO and $NH_2$-$C_{12}$-PMO. Figure S4b (SI) shows the TEM image in the direction parallel to the channels of the $NH_2$-$C_{16}$-PMO, supporting the hexagonal arrangement of the pores observed by PXRD and confirming the high order of these materials.

Solid-state $^{13}C$ CP MAS NMR and $^{29}Si$ CP MAS NMR spectra of $C_n$-PMO and $NH_2$-$C_n$-PMO materials are shown in Figures S5 (SI) and Figure 2, respectively. Solid-state $^{13}C$ CP MAS NMR spectra support the amination of $C_n$-PMOs materials. The pristine materials present a typical resonance at 133 ppm of the aromatic carbons as reported in the literature.[41] Tiny peaks can be detected in the region 0 to 50 ppm in the spectra of $C_{18}$-PMO sample, which are associated to the residual presence of non-extracted template molecules.

These resonances are no observed in the spectra of the other $C_n$-PMOs. The $^{13}C$ CP MAS NMR spectra of $NH_2$-$C_n$-PMO materials exhibit resonances at *ca*. 122, 133 and 150 ppm assigned to the $sp^2$ carbons of the phenylene ring. These values are in agreement with the results previously reported for the $NH_2$-$C_{18}$-PMO.[40] The $^{29}Si$ CP MAS NMR spectra of the $C_n$-PMO and $NH_2$-$C_n$-PMO exhibit peaks at *ca.* -81, -70 and -61 ppm attributed to $T^3$, $T^2$ and $T^1$ organosiliceous species [$T^m = RSi(OSi)_m(OH)_{3-m}$], respectively, which are illustrated in Figure 2.

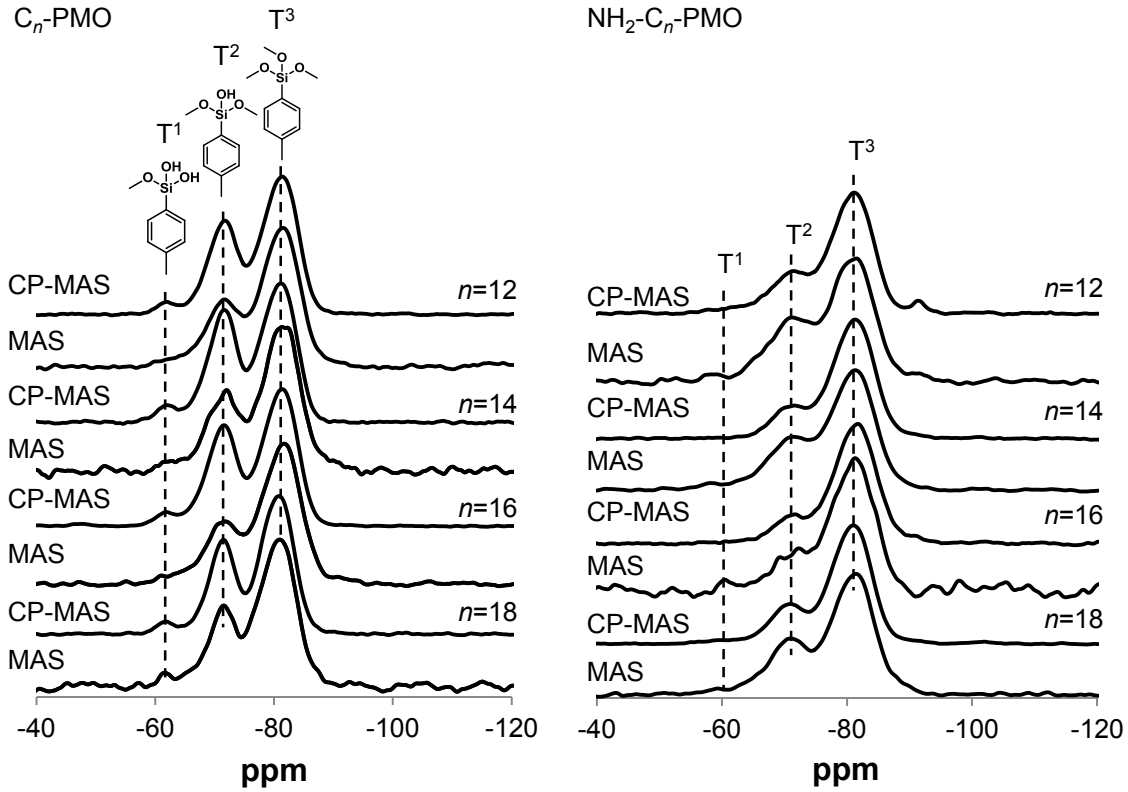


**Figure 2.** $^{29}Si$ CP-MAS and MAS NMR spectra of $C_n$-PMOs and $NH_2$-$C_n$-PMO. The observed resonances are assigned to the corresponding $T^m$ silanols species in the PMO materials.

The percentages of $T^m$ species in each material are calculated from the deconvolution of the $^{29}Si$ MAS NMR spectra, using the typical assumption of Gaussian distributions of isotropic chemical shifts for each type of $T^m$ species and are presented in

Table S1. Generally, the overlapping of $T^m$ resonances is observed, giving rise to small variations between best-fit intensity parameters and, hence, to uncertainties related with the relative populations of the $T^m$ sites. The degree of condensation varies between 66 and 71 % for the $C_n$-PMOs and between 66 and 74 % for the $NH_2$-$C_n$-PMO materials. No peaks attributable to $Q^n$ [$Q^n = Si(OSi)_n(OH)_{4-n}$] species were observed, proving that no carbon–silicon bond cleavage occurred during the amination of the PMO materials. The $^{15}N$ NMR spectra of the $NH_2$-$C_n$-PMO materials (not shown) display in all cases only a single peak corresponding to the aromatic amine at -325 ppm as observed before for $NH_2$-$C_{18}$-PMO and $NH_2$-$C_{12}$-PMO.[44,45] The success of the amination of the phenylene moieties in the PMOs was also verified by Fourier infrared transform (FTIR) spectroscopy, Figure S6 (SI).

Figure S7 (SI) presents the TGA analysis of the pristine and amine modified $C_n$-PMOs. The first weight loss observed below 100 ºC is related to desorption of physisorbed water. No weight loss from 100 to 300 ºC, which is due to the small quantity of remained surfactant, was detected for pure PMOs with exception of $C_{18}$-PMO (2% weight loss), confirming the $^{13}C$ CP MAS NMR results. The decomposition and release of the organic moieties from the framework takes place above 600 ºC in the parent $C_n$-PMOs. The introduction of the amine groups in the PMOs leads to a reduction of thermal stability from 600 to 400 ºC for all $NH_2$-$C_n$-PMOs as observed by TGA, Figure S7 (SI).

Table S2 (SI) displays the density of the amine group linked to the phenylene moieties into the PMOs materials. The PMO with the smallest pore size presents the lowest density of $NH_2$ groups. This probably occurs as a consequence of steric hindrance during the functionalization.

### 3.2. Experimental pure-component adsorption isotherms

Pure-component adsorption isotherms of $CO_2$ and $CH_4$ at 35 ºC on the $C_{12}$-PMOs, shown in terms of absolute amount adsorbed per unit mass of adsorbent ($q$), are displayed in Figure 3. The introduction of the amine group into the channels of the $C_{12}$-PMO leads to an increase in the adsorption of $CO_2$ (uppermost curves in Figure 3). Additionally, the adsorption of methane in the $NH_2$-$C_{12}$-PMO is slightly lower than in the as-synthesized material (lowermost curves in Figure 3).

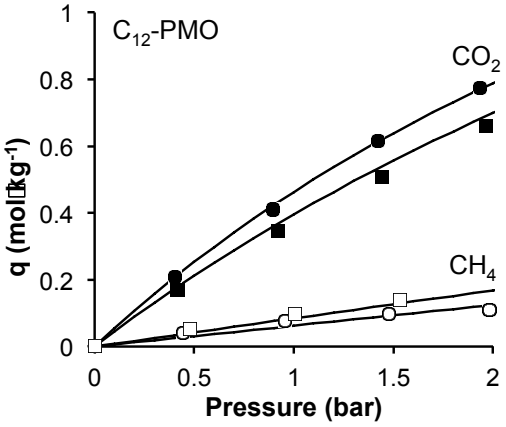


**Figure 3.** Adsorption equilibrium isotherms of pure $CO_2$ (closed symbols) and $CH_4$ (open symbols) molecules in the as-synthesized (squares) and amine functionalized (spheres) $C_{12}$-PMOs. Solid lines represent the fits to Langmuir model.

Table 3 depicted the calculated Henry's constants of adsorption for pure $CO_2$ and $CH_4$ molecules in the pristine and amine functionalized $C_n$-PMOs adsorbents. Considering the low $CH_4$ adsorption values obtained for all prepared PMOs, it is possible to generalize that these materials are weak $CH_4$ adsorbents. Additionally, the amination in the $C_{12}$-PMO provides an improvement in the adsorption of the material. It should be emphasized that this evidence is not observed for all $C_n$-PMOs. The amination of the $C_n$-PMOs is favoring the adsorption of $CO_2$ in the case of the materials with the smallest pores such as $NH_2$-$C_{12}$-

PMO and $NH_2$-$C_{14}$-PMO (Figure 3, Figure S8 and Table 3), while an opposite effect is observed in the materials with the largest pore sizes (cf. $NH_2$-$C_{16}$-PMO and $NH_2$-$C_{18}$-PMO). A systematic analysis of the features of these materials is necessary to understand other reasons besides pore size and BET surface area factors that may be influencing the adsorption profiles recorded in this work.

The Henry's constants of $C_{18}$-PMO, $C_{16}$-PMO, $C_{14}$-PMO and $C_{12}$-PMO for $CO_2$ are 0.40, 0.48, 0.41 and 0.46 $mol \cdot kg^{-1} \cdot bar^{-1}$ respectively (Table 3). As it can be seen, these values seem to be fairly independent of the pore size. Although the size of the pores can influence the distance between functional groups and, consequently, the Henry's constants, it is often observed that in materials with large pores, low-coverage adsorption is dominated by surface chemistry. As such, the variation of $K_H$ may be related with the concentration of silanols ($T^1$ and $T^2$ species, Figure 2), phenylene density and nitrogen density (in the case of the amine functionalized $C_n$-PMOs) of each material. The quantification of these characteristics for each material considered in this work is displayed in Table 3. The percentages of nitrogen and carbon were taken directly from elemental analyses. The percentage of silanol species was calculated from $^{29}Si$ MAS NMR by deconvolution of the $T^1$ and $T^2$ species in the NMR spectrum of each material (denoted as $T^1_{NMR}$ and $T^2_{NMR}$, Table S1, SI). As the percentages of siliceous and of oxygen species vary from sample to sample, the $T^m$ siliceous species percentage were converted to the percentage of $T^m$ siliceous species present in the sample (denoted here as $T^1_{SMP}$ and $T^2_{SMP}$) by combining the NMR results with the elemental analysis data. It is hypothesized that the $CO_2$ molecules interact more favorably with the $T^1$ and $T^2$ siliceous species in each sample. Therefore, the total percentage of siliceous species (denoted here as %Si-O) of each material (Table S2, SI) was calculated using the following Equation 3:

$$\%Si\text{-}O = \%Si + \%O = 100\% - (\%N + \%C + \%H) \quad \text{(Equation 3)}$$

The %Si-O, %N, %C and %H represent the sum of the percentages of silicon and oxygen, nitrogen, carbon and hydrogen,respectively, of each material, and are obtained from elemental analyses. Then the percentage of $T^m_{NMR}$ species was multiplied by the percentage of Si-O to obtain $\%T^m_{SMP}$. The evident correlation between the percentage of $T^m$ species in each sample and the corresponding $K_H^{CO2}$ values supports the hypothesis raised above.

**Table 3.** Comparison of structural and chemical properties of the as-synthesized and amine functionalized $C_n$-PMOs adsorbents with experimental Henry's constants of pure $CO_2$ and $CH_4$ adsorption, and the equilibrium selectivity.

| PMO | $d_P$[a] (nm) | % N[b] | % C[b] | % $T^1_{SMP}$[c] | % $T^2_{SMP}$[c] | $K_H^{CO2}$[d] (mol·kg$^{-1}$·bar$^{-1}$) | $K_H^{CH4}$[d] (mol·kg$^{-1}$·bar$^{-1}$) | $S$[e] |
|---|---|---|---|---|---|---|---|---|
| **$C_{18}$-PMO** | 3.70 | - | 38.39 | 1.17 | 15.99 | 0.400 | 0.074 | 5.40 |
| **$NH_2$-$C_{18}$-PMO** | 3.54 | 3.03 | 35.81 | 1.32 | 15.51 | 0.341 | 0.070 | 4.89 |
| **$C_{16}$-PMO** | 3.14 | - | 36.38 | 0.96 | 19.26 | 0.478 | 0.076 | 6.26 |
| **$NH_2$-$C_{16}$-PMO** | 3.14 | 3.16 | 32.12 | 1.14 | 14.86 | 0.416 | 0.078 | 5.31 |
| **$C_{14}$-PMO** | 2.80 | - | 38.56 | 1.41 | 18.43 | 0.414 | 0.083 | 4.98 |
| **$NH_2$-$C_{14}$-PMO** | 2.80 | 2.89 | 31.29 | 1.28 | 17.20 | 0.470 | 0.086 | 5.49 |
| **$C_{12}$-PMO** | 2.54 | - | 37.21 | 1.22 | 18.92 | 0.457 | 0.084 | 5.43 |
| **$NH_2$-$C_{12}$-PMO** | 2.41 | 2.58 | 31.57 | 0.77 | 20.61 | 0.560 | 0.062 | 8.97 |

[a]Pore width obtained from the BJH method with the corrected Kelvin equation, i.e. KJS–BJH method at the maximum of pore size distribution calculated on the basis of adsorption data. [b]Obtained directly from elemental analyses. Note that the percentage of carbon can be also calculated for clean non-functionalized phenylene-PMO as exemplified in the footnote of Table S2. [c]Calculated from the $^{29}$Si MAS NMR by deconvolution of the $T^1$ and $T^2$ species in the spectrum of each material. This percentage was converted to the percentage in the sample through the use of elemental analysis. [d]Henry's constants of adsorption, determined from fitting the experimental adsorption data to the Langmuir isotherm model; [e]Low-coverage adsorption selectivity for $CO_2$, estimated from the ratio of the pure component Henry's constants shown in the previous two columns.

The analysis of the data in Table 3 shows that the presence of $T^2$ silanol species in the PMO is correlated with the amount of adsorbed $CO_2$, i.e., in general the $K_H^{CO_2}$ augments with the increase of $\%T^2_{SMP}$. This observation is consistent with a picture that the presence of $^{29}Si$ $T^2$ silanol species in the PMO brings a positive effect on the adsorption of $CO_2$ by creating hydrogen bonds with the acidic $CO_2$. Curiously, $K_H^{CO_2}$ reduces with the increase of the percentage of the silanediol species, i.e., with the amount of silanols with $T^1$ environments (cf. Figure 2). This suggests that when two hydroxyl groups are linked to the same silicon atom, they are very probably establishing intramolecular bonds of the type O–H···O,[46] hence, less Si–O–H moieties are available to interact with $CO_2$. As the $T^1$ species content in the different PMO is inversely proportional to the $T^2$ species content (cf. Table S1, 1st and 2nd column), the amount of adsorbed $CO_2$ by each PMO is influenced mainly by the number of basic $T^2$ silanol species. The correlation between the percentage of $T^2_{SMP}$ silanol on each sample and the Henry constants is presented in Figure S9a.

The $CO_2$ molecules can also interact with the organic moieties but such interaction is expected to be much weaker than those with the silanol species. In fact, Martinez *et al.*[47] found through density functional theory (DFT) calculations that the interaction energy between $CO_2$ and silanols with the $T^2$ environment was twice that occurring between $CO_2$ and the organic bridges. Preliminary DFT calculations (PBE-D2 level of theory) employing a computational recipe and a PMO model similar to those used by Martinez et al.[47] show that $CO_2$ is positioned close to a $T^2$ silanol species in the pristine PMO material, as can be observed in Figure 4a. Although at low pressure it is not expected interaction between the organic bridges and $CO_2$ molecules, the presence of the organic moieties may contribute to

enhance the interaction of $CO_2$ with the $T^2$ silanols by interrupting long range hydrogen bond interaction within silanols.

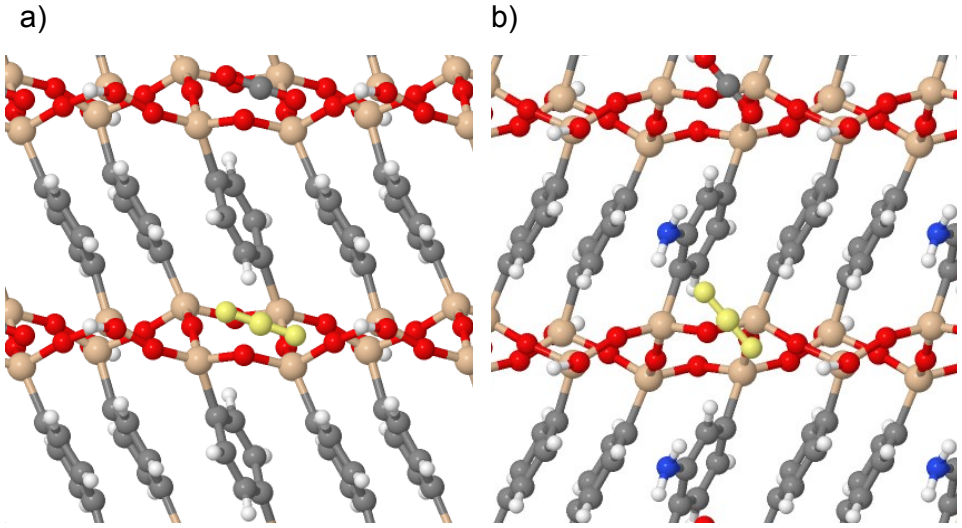


**Figure 4**. $CO_2$ preferential location on a) $C_n$-PMOs and b) $NH_2$-$C_n$-PMOs. The $CO_2$ is highlighted in yellow.

Therefore, at low pressure, the $CO_2$ molecules interact only with available silanols on the surface of the materials while regions close to the organic moieties will be populated only at high pressure. Based on these premises, we have tentatively defined a correlation equation (Equation 4) that may represent the number of $CO_2$ preferential adsorption sites in the non-aminated PMO materials, $f_{OH}$, as:

$$f_{OH} \cong \% \, T^2_{SMP} \, / \, \% \, C \qquad \text{(Equation 4)}$$

where % $T^2_{SMP}$ and % C correspond to the percentages of $T^2$ silanols and carbon atoms on the PMO material. The % C appears as uniformed weight factor of the materials. The $f_{OH}$ values for the non-aminated PMOs are compared in Table 4 with the Henry constants for the corresponding materials.

**Table 4.** Number of $CO_2$ preferential adsorption sites calculated with Equation 4 and Henry's constants of adsorption for pure $CO_2$ on the $C_n$-PMOs adsorbents.

| PMO | $f_{OH}$ (%$T^2_{SMP}$ / %C) | $K_H^{CO_2}$ (mol·kg$^{-1}$·bar$^{-1}$) |
|---|---|---|
| **$C_{18}$-PMO** | 0.42 | 0.40 |
| **$C_{16}$-PMO** | 0.53 | 0.48 |
| **$C_{14}$-PMO** | 0.48 | 0.41 |
| **$C_{12}$-PMO** | 0.51 | 0.46 |

Interestingly, the ordering of the calculated $f_{OH}$ values is identical to that of the Henry's constants of pure $CO_2$. This suggests that the properties used to establish the relationship in Equation 4 are the most important in defining the $CO_2$ adsorption affinities of the $C_n$-PMO, $n$ = 12, 14, 16, and 18, materials considered in this work.

In the case of the aminated materials, i.e., $NH_2$-$C_n$-PMOs, the calculation of the $f_{OH}$ values is more complicated, due to the existence of nearly 50% of phenylene moieties that could not be functionalized during the experimental syntheses. Moreover, the aminated phenylene motifs interact much more strongly with $CO_2$ molecules than the bare phenylene moieties. Thus, the aminated $C_n$-PMOs present different degrees of hydrophobicity and different degrees of acidity in the same material when compared with the pristine materials. Additionally, different interactions between amine groups, silanol species and phenylene moieties can occur due to the distribution of the amine groups on the walls of the materials.

These factors increase the degree of complexity in the determination of $f_{OH}$. Still, DFT calculations[45] for the adsorption of $CO_2$ on a periodic model of the walls of the aminated phenylene PMO, derived from the model developed by Martínez *et al*.[47] by substitution of a phenyl hydrogen atom with an amino group, show that the $CO_2$ adsorbate interacts preferentially with the isolated $T^2$ silanol species, in a bridging configuration where it also interacts with a neighboring amine group (cf. Figure 4b). So, the main difference to the corresponding non-aminated PMOs is the strength of the interaction, which is slightly higher in the aminated materials than in the pristine PMOs. In principle, this simultaneous interaction of the $CO_2$ with silanols and amine groups will have a greater probability of occurrence in materials having smaller pore sizes, because the pore curvature is expected to allow these two functional groups to be closer to each other than in the materials with larger pore sizes. Positively, our assumptions seem to be supported by the *b* affinity parameters (Table S3, SI), which are found to only increase upon amination in the case of the $C_{12}$ materials, to be similar in the case of $C_{14}$ PMOs, and to decrease in the cases of the $C_{16}$ and $C_{18}$ materials. So, in the case of the materials with the largest pore sizes, the coefficient related to the affinity between the sorbent and the sorbate decreases upon the amination reaction. Thus, we can approximate that, at low pressure, the number of sites for $CO_2$ adsorption in the aminated samples is identical to the number of $T^2$ type silanols. In fact, as it can be seen in Figure S8b, the percentage of $T^2_{SMP}$ silanol types on the aminated samples is correlated with the values of the Henry constants. In this way, Equation 4 can also be used to calculate the number of $CO_2$ preferential adsorption sites in the aminated PMO materials. The calculated $f_{OH}$ values for the $NH_2$-$C_n$-PMOs materials are compared in Table 5 with the Henry's constants of pure $CO_2$.

**Table 5.** Correlation of chemical properties with the calculated low-coverage adsorption capacities of pure $CO_2$ for the $NH_2$-$C_n$-PMOs adsorbents.

| PMO | $f_{OH}$ (%$T^2_{SMP}$ / %C) | $K_H^{CO_2}$ (mol·kg$^{-1}$·bar$^{-1}$) |
|---|---|---|
| **$NH_2$-$C_{18}$-PMO** | 0.43 | 0.34 |
| **$NH_2$-$C_{16}$-PMO** | 0.46 | 0.42 |
| **$NH_2$-$C_{14}$-PMO** | 0.55 | 0.47 |
| **$NH_2$-$C_{12}$-PMO** | 0.65 | 0.56 |

Encouragingly, as found for the as-synthesized materials, the latter quantities are in excellent qualitative agreement, again suggesting that the amounts of adsorbed $CO_2$ in these materials are correlated with the percentages of $T^2$ silanols divided by the % of carbon determined by EA, which is a normalizing factor. As expected, the discrepancies between the two quantities are larger in the aminated materials than in the as-synthesized ones because of the heterogeneous distribution of the amine groups and of possible formation of structural defects upon the amination reaction. Once again, the adsorption of carbon dioxide at low pressure in materials displaying a large variety of organic and inorganic adsorption sites can be described by a very simple correlation (Equation 4). This observation is a convincing sign of the local nature of the adsorption mechanism, which involves a quite limited number of surface atoms, and it is in agreement with recent theoretical studies on these materials.[47]

### 3.3. Comparison to other materials

The capacity of $NH_2$-$C_{12}$-PMO to capture carbon dioxide and methane is compared in Table 6 with the capacities reported in the literature for other classes of adsorbents, namely, metal organic frameworks (MOFs), zeolites, zeolitic imidazolate framework

(ZIFs), silicas, carbons and clays. Notice that data were determined at different temperatures with concomitant effects on the values of the capacities. For instance, in the case of the MAC (microwave activated carbon) material, a 20 % reduction in the $CO_2$ capacity is found on increasing temperature from 25 °C to 35 °C. A similar reduction (of 27 %) was also found for the $C_{18}$-PMO when enhancing the temperature from 25 °C to 35 °C. Although, the ratio of adsorption capacity of $CO_2/CH_4$ is improved with this increase of temperature. The results obtained for the PMO materials in this work were obtained at the 35 °C and a pressure of 1 atm.

**Table 6.** Capacities of different adsorbents in the $CO_2$ / $CH_4$ separation at 1 bar.

| Type | Materials | $CO_2$ capacity ($mol \cdot kg^{-1}$) | $CH_4$ capacity ($mol \cdot kg^{-1}$) | Temperature | $\frac{CO_2 \text{ capacity}}{CH_4 \text{ capacity}}$ |
|---|---|---|---|---|---|
| **Carbons** | MAC[19] | 2.13 | 0.98 | 25 ºC | 2.2 |
| | | 1.69 | 0.81 | 35 ºC | 2.1 |
| | Activated Carbon[48] | ≈2.1 | ≈0.9 | | 2.3 |
| **Clays** | PILC $Al_w$[27] | ≈0.40 | ≈0.07 | 25 ºC | 5.7 |
| **MOFs** | MOF-14(Cu)[49] | ≈2.50 | ≈1.00 | | 2.5 |
| | CPO-27-Ni[50] | ≈7.50 | ≈4.38 | | 1.7 |
| | CPO-27-Mg[50] | ≈8.75 | ≈4.29 | | 2.0 |
| | amino-MIL-53(Al)[51] | 1.96 | ≈0.30 | 30 ºC | 6.5 |
| **Silicas** | a-MCMBs[17] | 1.97 | 1.23 | 25 ºC | 1.6 |
| **Zeolites and ZIFs** | Hβ-zeolite[52] | 1.76 | 0.38 | 30 ºC | 4.6 |
| | Naβ-zeolite[52] | ≈2.80 | ≈0.70 | | 4.0 |
| | ZIF-7[4] | 2.34 | 0.13 | 25 ºC | 18.0 |
| | T-type zeolite[53] | ≈1.90 | ≈0.30 | 35 ºC | 6.3 |
| | LiX zeolite[48] | ≈3.90 | ≈0.69 | | 5.7 |
| | 13X zeolite[22] | ≈4.08 | ≈0.50 | | 8.2 |
| | Chabazite zeolite (**r2**KCHA)[54] | ≈3.70 | ≈1.10 | | 3.4 |
| **PMOs** | $C_{18}$-PMO | 0.49 | 0.11 | 25 °C | 4.5 |
| | | 0.36 | 0.07 | 35 ºC | 5.1 |
| | $NH_2$-$C_{12}$-PMO | 0.46 | 0.08 | | 5.8 |

The data in Table 6 show that the capacity of the $NH_2$-$C_{12}$-PMO material to adsorb either $CO_2$ or $CH_4$ is quite low when compared to the other materials, but the ratio between the capacities for $CO_2$ and $CH_4$ is among the best. Importantly, the capacity to adsorb

methane is very low which may be seen as very convenient for separation processes. If one compares the ratios of the capacities for capturing the two gases by different materials reported in literature with our best material ($NH_2$-$C_{12}$-PMO), measured at the same temperature and pressure (35 ºC, 1 atm), it is possible to verify that the $NH_2$-$C_{12}$-PMO material presents a relatively high capacity ratio, being superior than both MAC and activated carbon, 5.8 versus 2.1 and 2.3, respectively. Additionally, the capacity ratio of $NH_2$-$C_{12}$-PMO is similar to those obtained in most of zeolites presented in Table 6 at the same working conditions, showing that PMO materials incorporating different functionalities can be good candidates for $CO_2/CH_4$ separation processes.

To summarize, amine-modified phenylene PMOs with different pore sizes were successfully synthetized and characterized. All pristine and amine-modified phenylene PMO materials showed two-dimensional hexagonal symmetry (*p6mm*) lattice and molecular-scale periodicities observed by PXRD and TEM. It was evaluated the performance of the materials on adsorption of pure carbon dioxide and methane at 35 ºC at low pressure. The adsorption of $CO_2$ was much higher than that of $CH_4$, anticipating high $CO_2$ selectivity. Direct correlations between the amounts of $CO_2$ adsorbed and material pore sizes or specific surface areas were not found. In order to understand the differences obtained for the $CO_2$ adsorption within all materials, the Henry's constants of adsorption were determined, as well as their chemical features. A simple expression considering the the % of $T^2_{SMP}$ silanol species was found to provide a good prediction of the experimental Henry's law constants for pure $CO_2$ adsorption on each material. The adsorbent with the best chemical features to adsorb $CO_2$ was the $NH_2$-$C_{12}$-PMO, presenting a Henry constant of 0.56 $mol \cdot kg^{-1} \cdot bar^{-1}$ at 35 ºC. However, the corresponding Henry constant for $CH_4$ is

extremely low (0.06 $mol \cdot kg^{-1} \cdot bar^{-1}$ at 35 ºC), turning it potentially interesting for the separation of this gas from $CO_2$.

PMOs can be used as adsorbents with improved characteristics for $CO_2$ adsorption/separation from $CH_4$ at low pressure. For that, they should present high degree of silica condensation (high amounts of $T^2$ silanols and small quantities of $T^1$ silanols). In addition, the pore sizes and BET surfaces seem not to play a direct role on the adsorption capacities, our results may indicate the existence of an indirect relation. Thus, the pore size should affect the curvature of the pore, the degree of condensation and thus the silanol type content. This information may be used in the future to design more effective functionalized PMO materials for biogas upgrading.

## Supporting Information

All experimental details and data of -196 °C $N_2$-sorption isotherms, TEM, EA, $^{13}C$ solid-state NMR, FTIR, and pure $CO_2$ and $CH_4$ adsorption isotherms for all prepared materials are available free of charge via the Internet at http://pubs.acs.org/.

## Notes

The authors declare no competing financial interest.

## Acknowledgments

This work was developed in the scope of the project CICECO-Aveiro Institute of Materials POCI-01-0145-FEDER-007679 (Ref. FCT UID/CTM/50011/2013), financed by national funds through the FCT/MEC and when applicable co-financed by FEDER under the PT2020 Partnership Agreement,, project FCOMP-01-0124-FEDER-010345 (PTDC/EQU-EQU/099423/2008), FCT Programmes Ciência 2007 and Investigador FCT. Authors are also grateful to Dr. L. Mafra and Dr. R. Siegel for their support in the $^{15}N$ CP MAS analyses and to the National Network of electron microscopy and University of Aveiro: Project REDE/1509/RME/2005. MAOL acknowledges the grant SFRH/BD/80883/2011.

The authors gratefully acknowledge Dr. Moisés Pinto (University of Lisbon) and Dr. Ashleigh Fletcher (University of Strathclyde) for many fruitful discussions. This work is included in a collaborative project framed in the European MP1202: HINT COST action.

## References

(1) Harasimowicz, M.; Orluk, P.; Zakrzewska-Trznadel, G.; Chmielewski, A. G. Application of Polyimide Membranes for Biogas Purification and Enrichment. *J.*

*Hazard. Mater.* **2007**, *144*, 698–702.

(2) Favre, E.; Bounaceur, R.; Roizard, D. Biogas, Membranes and Carbon Dioxide Capture. *J. Memb. Sci.* **2009**, *328*, 11–14.

(3) Heile, S.; Rosenberger, S.; Parker, A.; Jefferson, B.; McAdam, E. J. Establishing the Suitability of Symmetric Ultrathin Wall Polydimethylsiloxane Hollow-Fibre Membrane Contactors for Enhanced $CO_2$ Separation during Biogas Upgrading. *J. Memb. Sci.* **2014**, *452*, 37–45.

(4) Wu, X.; Niknam Shahrak, M.; Yuan, B.; Deng, S. Synthesis and Characterization of Zeolitic Imidazolate Framework ZIF-7 for $CO_2$ and $CH_4$ Separation. *Micropor. Mesopor. Mater.* **2014**, *190*, 189–196.

(5) Sahoo, P. K.; John, M.; Newalkar, B. L.; Choudhary, N. V.; Ayappa, K. G. Filling Characteristics for an Activated Carbon Based Adsorbed Natural Gas Storage System. *Ind. Eng. Chem. Res.* **2011**, *50*, 13000–13011.

(6) Bhadra, S. J.; Farooq, S. Separation of Methane–Nitrogen Mixture by Pressure Swing Adsorption for Natural Gas Upgrading. *Ind. Eng. Chem. Res.* **2011**, *50*, 14030–14045.

(7) Jaramillo, P.; Matthews, H. S. Landfill-Gas-to-Energy Projects: Analysis of Net Private and Social Benefits. *Environ. Sci. Technol.* **2005**, *39*, 7365–7373.

(8) Knaebel, K.; Reinhold, H. Landfill Gas: From Rubbish to Resource. *Adsorption* **2003**, *9*, 87–94.

(9) Lohila, A.; Laurila, T.; Tuovinen, J. P.; Aurela, M.; Hatakka, J.; Thum, T.; Pihlatie, M.; Rinne, J.; Vesala, T. Micrometeorological Measurements of Methane and Carbon Dioxide Fluxes at a Municipal Landfill. *Environ. Sci. Technol.* **2007**, *41*, 2717–2722.

(10) Spigarelli, B. P.; Kawatra, S. K. Opportunities and Challenges in Carbon Dioxide Capture. *J. $CO_2$ Util.* **2013**, *1*, 69–87.

(11) Cavenati, S.; Grande, C. A.; Rodrigues, A. E. Removal of Carbon Dioxide from Natural Gas by Vacuum Swing Adsorption. *Energy Fuels* **2006**, *20*, 2648–2659.

(12) Bae, Y. S.; Snurr, R. Q. Development and Evaluation of Porous Materials for Carbon Dioxide Separation and Capture. *Angew. Chemie* **2011**, *50*, 11586–11596.

(13) Chaemchuen, S.; Kabir, N. A.; Zhou, K.; Verpoort, F. Metal–organic Frameworks for Upgrading Biogas via $CO_2$ Adsorption to Biogas Green Energy. *Chem. Soc. Rev.* **2013**, *42*, 9304–9332.

(14) Rodrigues, A. E.; Grande, C. A. Biogas to Fuel by Vacuum Pressure Swing Adsorption I. Behavior of Equilibrium and Kinetic-Based Adsorbents. *Ind. Eng. Chem. Res.* **2007**, *46*, 4595–4605.

(15) Babarao, R.; Hu, Z.; Jiang, J.; Chempath, S.; Sandler, S. I. Storage and Separation of $CO_2$ and CH4 in Silicalite, C 168 Schwarzite, and IRMOF-1: A Comparative Study from Monte Carlo Simulation. *Langmuir* **2007**, *23*, 659–666.

(16) Kim, M. B.; Bae, Y. S.; Choi, D. K.; Lee, C. H. Kinetic Separation of Landfill Gas by a Two-Bed Pressure Swing Adsorption Process Packed with Carbon Molecular Sieve: Nonisothermal Operation. *Ind. Eng. Chem. Res.* **2006**, *45*, 5050–5058.

(17) Peng, X.; Wang, W.; Xue, R.; Shen, Z. Adsorption Separation of $CH_4/CO_2$ on Mesocarbon Microbeads: Experiment and Modeling. *AIChE J.* **2006**, *52*, 994–1003.

(18) Goetz, V.; Pupier, O.; Guillot, A. Carbon Dioxide-Methane Mixture Adsorption on Activated Carbon. *Adsorption* **2006**, *12*, 55–63.

(19) Yi, H.; Li, F.; Ning, P.; Tang, X.; Peng, J.; Li, Y.; Deng, H. Adsorption Separation of $CO_2$, $CH_4$, and $N_2$ on Microwave Activated Carbon. *Chem. Eng. J.* **2013**, *215-216*,

635–642.

(20) D'Alessandro, D. M.; Smit, B.; Long, J. R. Carbon Dioxide Capture: Prospects for New Materials. *Angew. Chemie - Int. Ed.* **2010**, *49*, 6058–6082.

(21) Pirngruber, G. D.; Hamon, L.; Bourrelly, S.; Llewellyn, P. L.; Lenoir, E.; Guillerm, V.; Serre, C.; Devic, T. A Method for Screening the Potential of MOFs as $CO_2$ Adsorbents in Pressure Swing Adsorption Processes. *ChemSusChem* **2012**, *5*, 762–776.

(22) Cavenati, S.; Grande, C. A.; Rodrigues, A. E. Adsorption Equilibrium of Methane, Carbon Dioxide, and Nitrogen on Zeolite 13X at High Pressures. *J. Chem. Eng. Data* **2004**, *49*, 1095–1101.

(23) Li, P.; Handan Tezel, F. Adsorption Separation of $N_2$, $O_2$, $CO_2$ and $CH_4$ Gases by β-Zeolite. *Microporous Mesoporous Mater.* **2007**, *98*, 94–101.

(24) Leyssale, J.-M.; Papadopoulos, G. K.; Theodorou, D. N. Sorption Thermodynamics of $CO_2$, $CH_4$, and Their Mixtures in the ITQ-1 Zeolite as Revealed by Molecular Simulations. *J. Phys. Chem. B* **2006**, *110*, 22742–22753.

(25) First, E. L.; Hasan, M. M. F.; Floudas, C. A. Discovery of Novel Zeolites for Natural Gas Purification Through Combined Material Screening and Process Optimization. *AIChE J.* **2014**, *60*, 31–33.

(26) Pinto, M. L.; Pires, J.; Rocha, J. Porous Materials Prepared from Clays for the Upgrade of Landfill Gas. *J. Phys. Chem. C.* **2008**, *112*, 14394–14402.

(27) Pires, J.; Saini, V. K.; Pinto, M. L. Studies on Selective Adsorption of Biogas Components on Pillared Clays: Approach for Biogas Improvement. *Environ. Sci. Technol.* **2008**, *42*, 8727–8732.

(28) Xue, Q.; Liu, Y. Mixed-Amine Modified SBA-15 as Novel Adsorbent of $CO_2$

Separation for Biogas Upgrading. *Sep. Sci. Technol.* **2011**, *46*, 679–686.

(29) Liu, X.; Zhou, L.; Fu, X.; Sun, Y.; Su, W.; Zhou, Y. Adsorption and Regeneration Study of the Mesoporous Adsorbent SBA-15 Adapted to the Capture/Separation of $CO_2$ and $CH_4$. *Chem. Eng. Sci.* **2007**, *62*, 1101–1110.

(30) García, E. J.; Pe, J.; Pirngruber, G. D.; Jallut, C.; Palomino, M.; Rey, F.; Valencia, S. Tuning the Adsorption Properties of Zeolites as Adsorbents for $CO_2$ Separation : Best Compromise between the Working Capacity and Selectivity. *Ind. Eng. Chem. Res.*, **2014**, *53*, 9860–9874**.**

(31) Asefa, T.; MacLachlan, M. J.; Coombs, N.; Ozin, G. A. Periodic Mesoporous Organosilicas with Organic Groups inside the Channel Walls. *Nature* **1999**, *402*, 867–871.

(32) Inagaki, S.; Guan, S.; Fukushima, Y.; Ohsuna, T. Novel Mesoporous Materials with a Uniform Distribution of Organic Groups and Inorganic Oxide in Their Frameworks. *J. Am. Chem. Soc.* **1999**, *121*, 9611–9614.

(33) Melde, B.; Holland, B.; Blanford, C.; Stein, A. Mesoporous Sieves with Unified Hybrid Inorganic/organic Frameworks. *Chem. Mater.* **1999**, *18*, 3302–3308.

(34) Van der Voort, P.; Esquivel, D.; De Canck, E.; Goethals, F.; Van Driessche, I.; Romero-Salguero, F. J. Periodic Mesoporous Organosilicas: From Simple to Complex Bridges; a Comprehensive Overview of Functions, Morphologies and Applications. *Chem. Soc. Rev.* **2013**, *42*, 3913–3955.

(35) Ferreira, P.; Bispo, C.; Lourenço, M. A. O.; Gomes, J. R. B.; Bion, N.; Vigier, K.; Jérôme, F. Making Periodic Mesoporous Organosilicas Functional Materials. In *Comprehensive guide for mesoporous materials, volume 4: application and commercialization*; Aliofkhazraei, M., Ed.; 2015; pp 261–295.

(36) Hoffmann, F.; Fröba, M. Vitalising Porous Inorganic Silica Networks with Organic Functions-PMOs and Related Hybrid Materials. *Chem. Soc. Rev.* **2011**, *40*, 608–620.

(37) Camarota, B.; Ugliengo, P.; Garrone, E.; Arean, C. O.; Delgado, M. R.; Inagaki, S.; Onida, B. IR and Computational Characterization of CO Adsorption on a Model Surface, the Phenylene Periodic Mesoporous Organosilca with Crystalline Walls. *J. Phys. Chem. C* **2008**, *112*, 19560–19567.

(38) Sim, K.; Lee, N.; Kim, J.; Cho, E.-B.; Gunathilake, C.; Jaroniec, M. $CO_2$ Adsorption on Amine-Functionalized Periodic Mesoporous Benzenesilicas. *ACS Appl. Mater. Interfaces* **2015**, *7*, 6792–6802.

(39) Bion, N.; Ferreira, P.; Valente, A.; Gonçalves, I. S.; Rocha, J. Ordered Benzene-Silica Hybrids with Molecular-Scale Periodicity in the Walls and Different Mesopore Sizes. *J. Mater. Chem.* **2003**, *13*, 1910–1913.

(40) Ohashi, M.; Kapoor, M. P.; Inagaki, S. Chemical Modification of Crystal-like Mesoporous Phenylene-Silica with Amino Group. *Chem. Commun.* **2008**, *7*, 841–843.

(41) Inagaki, S.; Guan, S.; Ohsuna, T.; Terasaki, O. An Ordered Mesoporous Organosilica Hybrid Material with a Crystal-like Wall Structure. *Nature* **2002**, *416*, 304–307.

(42) Corriu, R. J. P.; Moreau, J. J. E.; Thepot, P.; Chi Man, M. W. New Mixed Organic-Inorganic Polymers: Hydrolysis and Polycondensation of Bis(trimethoxysilyl) Organometallic Precursors. *Chem. Mater.* **1992**, *4*, 1217–1224.

(43) Jorge, M.; Fischer, M.; Gomes, J. R. B.; Siquet, C.; Santos, J. C.; Rodrigues, A. E. Accurate Model for Predicting Adsorption of Olefins and Paraffins on MOFs with Open Metal Sites. *Ind. Eng. Chem. Res.* **2014**, *53*, 15475–15487.

(44) Lourenço, M. A. O.; Siegel, R.; Mafra, L.; Ferreira, P. Microwave Assisted N-Alkylation of Amine Functionalized Crystal-like Mesoporous Phenylene-Silica. *Dalton Trans.* **2013**, *42*, 5631-5634.

(45) Lourenço, M. A. O.; Siquet, C.; Sardo, M.; Pires, J.; Mafra, L.; Jorge, M.; Pinto, M. L.; Ferreira, P.; Gomes, J. R. B. Interaction of $CO_2$ and $CH_4$ with Functionalized Periodic Mesoporous Phenylene–silica: Periodic DFT Calculations and Gas Adsorption Measurements. *J. Phys. Chem. C* **2016,** *120*, 3863−3875.

(46) Jal, P. K.; Patel, S.; Mishra, B. K. Chemical Modification of Silica Surface by Immobilization of Functional Groups for Extractive Concentration of Metal Ions. *Talanta* **2004**, *62*, 1005–1028.

(47) Martinez, U.; Pacchioni, G. Interaction of CO, $CO_2$ and $CH_4$ with Mesoporous Organosilica: Periodic DFT Calculations with Dispersion Corrections. *Micropor. Mesopor. Mater.* **2010**, *129*, 62–67.

(48) Park, Y.; Moon, D.-K.; Kim, Y.-H.; Ahn, H.; Lee, C.-H. Adsorption Isotherms of $CO_2$, CO, $N_2$, $CH_4$, Ar and $H_2$ on Activated Carbon and Zeolite LiX up to 1.0 MPa. *Adsorption* **2014**, *20*, 631–647.

(49) Karra, J. R.; Grabicka, B. E.; Huang, Y.-G.; Walton, K. S. Adsorption Study of $CO_2$, $CH_4$, $N_2$, and $H_2O$ on an Interwoven Copper Carboxylate Metal-Organic Framework (MOF-14). *J. Colloid Interface Sci.* **2013**, *392*, 331–336.

(50) Dietzel, P. D. C.; Besikiotis, V.; Blom, R. Application of Metal–organic Frameworks with Coordinatively Unsaturated Metal Sites in Storage and Separation of Methane and Carbon Dioxide. *J. Mater. Chem.* **2009**, *19*, 7362-7370.

(51) Peter, S. A.; Baron, G. V.; Gascon, J.; Kapteijn, F.; Denayer, J. F. M. Dynamic Desorption of $CO_2$ and $CH_4$ from Amino-MIL-53(Al) Adsorbent. *Adsorption* **2013**,

*19*, 1235–1244.

(52) Xu, X.; Zhao, X.; Sun, L.; Liu, X. Adsorption Separation of Carbon Dioxide, Methane, and Nitrogen on Hβ and Na-Exchanged β-Zeolite. *J. Nat. Gas Chem.* **2008**, *17*, 391–396.

(53) Rad, M. D.; Fatemi, S.; Mirfendereski, S. M. Development of T Type Zeolite for Separation of $CO_2$ from $CH_4$ in Adsorption Processes. *Chem. Eng. Res. Des.* **2012**, *90*, 1687–1695.

(54) Shang, J.; Li, G.; Singh, R.; Gu, Q.; Nairn, K. M.; Bastow, T. J.; Medhekar, N.; Doherty, C. M.; Hill, A. J.; Liu, J. Z.; Webley, P. A. Discriminative Separation of Gases by a "Molecular Trapdoor" Mechanism in Chabazite Zeolites. *J. Am. Chem. Soc.* **2012**, *134*, 19246–19253.

# Table Contents Graph